

Cite this: DOI: 00.0000/xxxxxxxxxx

Received Date  
Accepted Date

DOI: 00.0000/xxxxxxxxxx

## Self-Adaptive Real-Time Time-Dependent Density Functional Theory for Core Excitations

Linfeng Ye, Hao Wang\*, Yong Zhang, and Wenjian Liu\*

Real-time time-dependent density functional theory (RT-TDDFT) can in principle access all excitations of a many-electron system exposed to a narrow pulse. However, this requires an accurate and efficient propagator for the numerical integration of the time-dependent Kohn-Sham equation. While a low-order time propagator is already sufficient for the low-lying valence excitations, it is no longer the case for the core excitations of systems even composed only of light elements, for which the use of a high-order propagator is indispensable. It is then crucial to choose a largest possible time step and a shortest possible simulation time, so as to reduce the computational cost. To this end, we propose here a robust AutoPST approach to determine automatically (Auto) the propagator (P), step (S), and time (T) for relativistic RT-TDDFT simulations of core excitations.

### 1 Introduction

Triggered by the development of advanced synchrotron light sources and X-ray free electron lasers, X-ray absorption spectroscopy (XAS) has become an increasingly important technique for probing local electronic and geometric structure of matter. In XAS, innermost core electrons are excited to bound valence or continuum states in energetically distinct absorption edges, which are conventionally labeled according to the origins of the electronic transitions ( $K$ -edge for  $1s$ ,  $L_1$ -edge for  $2s$ ,  $L_2$ -edge for  $2p_{1/2}$ , and  $L_3$ -edge for  $2p_{3/2}$ , etc). There are two main regions in an XAS spectrum, X-ray absorption near-edge structure (XANES) near the rising edge with sharp resonance peaks and extended X-ray absorption fine structure (EXAFS) after the XANES region with gentle oscillations. The former provides electronic fingerprints of a particular atom (e.g., oxidation state, coordination, and bonding, etc), whereas the latter gives structural information about neighboring atoms (e.g., identity, distances, and coordination/solvation shells, etc). While the essential quantities (scattering amplitudes and phase shifts) in EXAFS can well be modeled already by a simple, damped spherical photoelectron wave function approximation, the complicated features of XANES spectra require more sophisticated treatments<sup>1</sup>, among which both static and time-dependent density functional theory (TDDFT) are widely adopted due to their good tradeoff between accuracy and efficiency. The former is commonly referred to as delta self-consistent field ( $\Delta$ SCF) and has a very appealing feature: orbital relaxation (which is of vast importance for core excitations) is

fully accounted for by SCF calculation of each core excited configuration. In particular, full spin adaptation can be achieved within the framework of multi-state DFT<sup>2–5</sup>. Yet, such one-by-one calculations of core excited states may not always be possible due to the non-Aufbau nature, given the availability of many algorithms<sup>6–16</sup>. In contrast, TDDFT can access all core excited states in one shot, by either diagonalization as in linear response (LR) TDDFT<sup>17–29</sup> or spectral analysis of the time signal generated by real-time (rt) TDDFT<sup>30–38</sup>. Yet, both LR-TDDFT and RT-TDDFT lacks orbital relaxation, thereby yielding XANES spectra that usually have large shifts as compared to the experimental ones. Since core excitations look very much like charge transfer excitations, it is clear that such large shifts can be alleviated to a large extent by using tuned range-separated functionals<sup>32,39,40</sup>. Anyhow, peak separations predicted by LR-TDDFT and RT-TDDFT are usually very good. As such, such one-for-all approaches are much more appealing than the one-by-one  $\Delta$ SCF approaches, at least from the computational point of view. Naturally, the relativistic counterparts of LR-TDDFT<sup>41–56</sup> or RT-TDDFT<sup>57–64</sup> should be invoked to account for relativistic effects, which are sizable already for core excitations even of very light elements. As for nonrelativistic/relativistic LR-TDDFT and RT-TDDFT themselves, LR-TDDFT is certainly advantageous over RT-TDDFT in accessing dark states (which are often important for, e.g., excited energy/charge transfers) as well as in the assignment of excited states due to the availability of CIS (configuration interaction singles) type of state eigenvectors<sup>65</sup>, especially when full molecular symmetry is employed<sup>66</sup>. Moreover, there exist very robust algorithms<sup>67–69</sup> that can access directly the core excited states as interior roots of the LR-TDDFT eigenvalue problem, without the need to invoke the so-called core-valence separation<sup>18–22</sup>, a very good approximation though<sup>70</sup>. Nevertheless, RT-TDDFT has the following

*Qingdao Institute for Theoretical and Computational Sciences, Institute of Frontier and Interdisciplinary Science, Shandong University, Qingdao, Shandong 266237, China; E-mail: wanghaosd@sdu.edu.cn; liuwj@sdu.edu.cn*

advantages as compared to LR-TDDFT: (1) only the exchange-correlation (XC) potential is needed, requiring no response of the XC potential, (2) the entire absorption spectrum can be obtained at once, via a single spectral analysis of the time-dependent dipole moment, (3) the memory footprint is only about one/two times that of the relativistic/nonrelativistic ground-state DFT calculation, thereby avoiding the memory bottleneck of LR-TDDFT resulting from the use of a large number of trial vectors during the iterative partial diagonalization, and (4) RT-TDDFT has the capability of accessing dynamical properties beyond the linear response regime. Because of these, RT-TDDFT has gained great popularity in the last decades.

From the computational point of view, the very first issue of RT-TDDFT is how to design a suitable propagator for the numerical integration of the underlying time-dependent Kohn-Sham equation (TDKS). While a low-order propagator<sup>71–73</sup> (e.g., the second-order Magus propagator (MP2)<sup>74</sup>) is already sufficient for the low-lying valence excitations, it is no longer the case for the core excitations of systems even composed only of light elements: a low-order propagator requires an exceedingly small time step to achieve a sufficient accuracy. The simulation is then much less efficient than the use of a higher-order propagator along with a larger time step. It is found here that, for the same accuracy (< 0.05 eV), the fourth-order optimized commutator-free exponential time-propagator (oCFET4)<sup>75</sup> is most efficient among the tested high-order propagators (including MPn<sup>74,76</sup>, CFETn<sup>77</sup>, and oCFETn<sup>75</sup> with n=4, 6) and can hence be regarded as a ‘just good enough’ high-order time propagator for core excitations. However, this is true only when it is combined with the EPEP3 (exponential prediction of density matrix and exponential correction of density matrix at three Gauss-Legendre points) type of predictor-corrector proposed here. Moreover, very robust linear relations and alias-free conditions for automatic determination of the largest possible time step as well as a good estimate of the shortest possible total simulation time will be established to automate the EPEP3@oCFET4/RT-TDDFT simulations of XASNES spectra. Because of the automated nature, the algorithms will be dubbed collectively as AutoPST (automated determination of propagator, step, and time), which can further be combined with full molecular symmetry<sup>66</sup>. To make the presentation complete, we first recapitulate the TDKS in Sec. 2.1 and then discuss the implementation of oCFET4 in Sec. 2.2 and EPEP3 in Sec. 2.3, where the closely related CFET4<sup>77</sup> and EPEP2 are also presented for comparison. The automated determination of time step is detailed in Sec. 2.4. Illustrative examples are then provided in Sec. 3 to reveal the performance of the proposed AutoPST approach. Some concluding remarks are finally made in Sec. 4.

## 2 Integration of TDKS

### 2.1 TDKS

RT-TDDFT amounts to integrating numerically the TDKS equation, followed by a spectral analysis to extract information on the electronic transitions. Under the adiabatic approximation, the TDKS equation discretized in a time-independent, orthonormal

basis  $\{\chi_\mu\}$  can be written as

$$i \frac{d}{dt} \mathbf{P}(t) = [\mathbf{F}(t), \mathbf{P}(t)], \quad \mathbf{F}(t) = \mathbf{F}_0(t) + \mathbf{V}^{(1)}(t), \quad (1)$$

which is also called Liouville-von Neumann equation for the evolution of the one-particle density matrix (1PDM)  $\mathbf{P}(t)$ . Here,  $\mathbf{F}_0(t)$  is the matrix representation of the field-free KS Hamiltonian at time  $t$ ,

$$\mathbf{F}_0(t) = T + V_{\text{nuc}} + V_h[\rho(t)] + c_x \Sigma_x[\gamma(t)] + c_{\text{xc}} V_{\text{xc}}[\rho(t)], \quad (2)$$

$$\rho(\mathbf{r}, t) = \sum_{\mu\nu} \chi_\mu^\dagger(\mathbf{r}) \chi_\nu(\mathbf{r}) P_{\nu\mu}(t),$$

$$\gamma(\mathbf{r}, \mathbf{r}', t) = \sum_{\mu\nu} \chi_\nu(\mathbf{r}) \chi_\mu^\dagger(\mathbf{r}') P_{\nu\mu}(t), \quad (3)$$

which is composed of the kinetic energy operator  $T$  (nonrelativistic or relativistic<sup>78,79</sup>), (static) nuclear attraction  $V_{\text{nuc}}$ , Hartree potential  $V_h$ , exact exchange potential  $\Sigma_x$ , and XC potential  $V_{\text{xc}}$ . The scaling coefficients  $c_x$  and  $c_{\text{xc}}$  denote the respective portions of  $\Sigma_x$  and  $V_{\text{xc}}$  included in the chosen hybrid functional. As for the time-dependent external field, we consider here simply a delta-perturbation

$$\varepsilon(\mathbf{r}, t) = \kappa \mathbf{n} \delta(t), \quad (4)$$

where  $\kappa$  and  $\mathbf{n}$  represent the field strength and polarization unit vector, respectively. The interaction operator  $\mathbf{V}^{(1)}(t)$  in Eq. (1) then reads (under the dipole approximation)

$$\mathbf{V}^{(1)}(t) = \tilde{\mathbf{V}}^{(1)} \delta(t), \quad \tilde{V}_{\mu\nu}^{(1)} = \kappa \sum_{\alpha=x,y,z} \langle \chi_\mu | r_\alpha | \chi_\nu \rangle n_\alpha. \quad (5)$$

Given an initial value  $\mathbf{P}(t_0)$ , the solution of Eq. (1) can formally be written as

$$\mathbf{P}(t) = \mathbf{U}(t, t_0) \mathbf{P}(t_0) \mathbf{U}^\dagger(t, t_0), \quad (6)$$

where  $\mathbf{U}(t, t_0)$  takes the following form

$$\mathbf{U}(t, t_0) = \mathcal{T} \exp \left\{ -i \int_{t_0}^t \mathbf{F}[\tau] d\tau \right\} \quad (7)$$

$$= \sum_{n=0}^{\infty} \frac{(-i)^n}{n!} \int_{t_0}^t d\tau_1 \int_{t_0}^{\tau_1} d\tau_2 \cdots \int_{t_0}^{\tau_{n-1}} d\tau_n \mathcal{T}[\mathbf{F}(\tau_1) \mathbf{F}(\tau_2) \cdots \mathbf{F}(\tau_n)]. \quad (8)$$

Here,  $\mathcal{T}$  is the time-ordering operator accounting for the fact that the KS matrices at different times do not commute. In practice, the time interval  $t - t_0$  will be split into  $N$  slices with equal length  $\Delta t$ , which amounts to splitting  $\mathbf{U}(t, t_0)$  as

$$\mathbf{U}(t, t_0) = \prod_{k=0}^{N-1} \mathbf{U}(t_{k+1}, t_k), \quad t_k = t_0 + k \Delta t. \quad (9)$$

In particular,  $\mathbf{U}(0^+, 0^-)$  takes a very simple for the delta-perturbation (5),

$$\mathbf{U}(0^+, 0^-) = \exp(-i \tilde{\mathbf{V}}^{(1)}), \quad (10)$$

which can readily be obtained from Eq. (7) by noticing that  $\mathbf{F}_0(\tau)$  does not change during the infinitely small time interval  $[0^-, 0^+]$ ,

such that only the  $\delta(t)$  term contributes to the time integral (see Ref. 57 for a more rigorous derivation). This suggests that a perturb-then-propagate procedure<sup>57,80,81</sup> can be invoked for the evolution of  $\mathbf{P}(t)$ , viz.,

$$\mathbf{P}(t) = \mathbf{U}(t, 0^+) \mathbf{P}(0^+), \quad (11)$$

$$\mathbf{P}(0^+) = \exp(-i\tilde{\mathbf{V}}^{(1)}) \mathbf{P}(0^-) \exp(i\tilde{\mathbf{V}}^{(1)}), \quad (12)$$

where  $\mathbf{P}(0^-)$  refers to the 1PDM in the absence of the external field.

Now the crucial point is how to parameterize the local evolution operators  $\mathbf{U}(t_{k+1}, t_k)$ . It should be clear from the outset that the various low-order schemes<sup>71-73</sup> are only appropriate for the lowest part of the TDKS spectra, for they would require exceedingly small time steps to be stable and accurate enough for the high-end part of the TDKS spectra. After extensive experiments, it is learned here that the oCFET4 with three exponentials<sup>75</sup> performs much better than MP4<sup>74,76</sup> in both accuracy and efficiency. Even higher-order propagators (MP6<sup>76</sup>, CFET6<sup>77</sup>, and oCFET6<sup>75</sup>, etc) are too expensive to be practical. For comparison, the closely related CFET4 with two exponentials<sup>77</sup> is also presented here. Both oCFET4 and CFET4 are unitary by construction, thereby conserving time reversal symmetry as well as the trace, hermiticity, and idempotency of  $\mathbf{P}(t)$ . However, strictly speaking, they are appropriate only for cases where the Hamiltonians governing the dynamics are time independent. For a time-dependent Hamiltonian as in RT-TDDFT, they have to be combined with some predictor-correctors to account for the inherent non-autonomy.

## 2.2 CFET4 and oCFET4

The Magnus expansion<sup>74,76</sup> has to be introduced first to make the presentation of CFET<sup>77</sup> clear. Briefly, the Magnus expansion amounts to replacing the complicated time-ordered integration

$$\mathbf{U}(t_{k+1}, t_k) = \mathcal{T} \exp \left[ \int_{t_k}^{t_{k+1}} \mathbf{A}(\tau) d\tau \right], \quad \mathbf{A}(\tau) = -i\mathbf{F}(\tau), \quad (13)$$

with a time-unordered exponential of an infinite series

$$\mathbf{U}(t_{k+1}, t_k) = \exp[\Omega(t_{k+1}, t_k)] \quad (14)$$

$$= \exp \left[ \sum_{l=1}^{\infty} \varepsilon^l \Omega_l(t_{k+1}, t_k) \right]_{\varepsilon=1}, \quad (15)$$

where the first two wave operators can readily be obtained as

$$\Omega_1(t_{k+1}, t_k) = \int_{t_k}^{t_{k+1}} d\tau \mathbf{A}(\tau), \quad (16)$$

$$\Omega_2(t_{k+1}, t_k) = \frac{1}{2} \int_{t_k}^{t_{k+1}} d\tau_1 \int_{t_k}^{\tau_1} d\tau_2 [\mathbf{A}(\tau_1), \mathbf{A}(\tau_2)]. \quad (17)$$

To evaluate the above time integrals, a Taylor expansion of  $\mathbf{A}(\tau)$  around the midpoint  $t_{1/2} = t_k + \Delta t/2$  can first be made,

$$\mathbf{A}(\tau) = \sum_{j=0}^{\infty} \mathbf{a}_j (\tau - t_{1/2})^j, \quad \mathbf{a}_j = \frac{1}{j!} \left. \frac{d^j \mathbf{A}(\tau)}{d\tau^j} \right|_{\tau=t_{1/2}}. \quad (18)$$

Further denoting  $\alpha_i = \mathbf{a}_{i-1} \Delta t^i$ , it can be shown<sup>76</sup> that only  $\{\alpha_i\}_{i=1}^s$  are needed to construct a wave operator  $\Omega^{[2s]}$  that is correct up to order  $\mathcal{O}(\Delta t^{2s})$ . Specifically,

$$\Omega^{[2]}(t_{k+1}, t_k) = \alpha_1, \quad (19)$$

$$\Omega^{[4]}(t_{k+1}, t_k) = \alpha_1 - \frac{1}{12} [\alpha_1, \alpha_2]. \quad (20)$$

To facilitate the numerical evaluation of  $\{\alpha_i\}_{i=1}^s$ , one can first define the following moments of  $\mathbf{A}(\tau)$

$$\mathbf{A}^{(i-1)} = \frac{1}{\Delta t^{i-1}} \int_{t_k}^{t_{k+1}} (\tau - t_{1/2})^{i-1} \mathbf{A}(\tau) d\tau, \quad i \in [1, s], \quad (21)$$

$$= \Delta t \int_0^1 (\tau - \frac{1}{2})^{i-1} \mathbf{A}(t_k + \tau \Delta t) d\tau, \quad (22)$$

$$= \Delta t \sum_{j=1}^n Q_{ij}^{(s,n)} \mathbf{A}_j^{[2s]} + \mathcal{O}(\Delta t^{2s+1}), \quad (23)$$

$$\mathbf{A}_j^{[2s]} = \mathbf{A}(t_k + c_j^{[2s]} \Delta t), \quad Q_{ij}^{(s,n)} = w_j^{[2s]} (c_j^{[2s]} - \frac{1}{2})^{i-1}, \quad (24)$$

where  $w_j^{[2s]}$  and  $c_j^{[2s]}$  are the weights and nodes of a quadrature required to evaluate  $\mathbf{A}^{(0)}$  correctly up to order  $2s$ , which are applied to the other moments  $\mathbf{A}^{(i)}$  as well. Inserting Eq. (18) into Eq. (21) leads to

$$\mathbf{A}^{(i-1)} = \sum_{j=1}^s (T^{(s)})_{ij} \alpha_j, \\ (T^{(s)})_{ij} = \frac{1 + (-1)^{i+j}}{(i+j-1) 2^{i+j-1}}, \quad i \in [1, s]. \quad (25)$$

Combining Eqs. (23) and (25) then gives rise to the general expression for  $\{\alpha_j\}_{j=1}^s$

$$\alpha_j = \Delta t \sum_{k=1}^n g_{jk} \mathbf{A}_k^{[2s]}, \quad g_{jk} = [(T^{(s)})^{-1} \mathbf{Q}^{(s,n)}]_{jk}, \quad j \in [1, s]. \quad (26)$$

Consider the Gauss-Legendre quadrature. It is obvious that only one grid point is needed for the second-order wave operator  $\Omega^{[2]}$ , i.e.,  $w_1^{[2]} = 1$  and  $c_1^{[2]} = \frac{1}{2}$ . We then have  $Q^{(1,1)} = 1$  and  $(T^{(1)})^{-1} = 1$  and hence

$$\Omega^{[2]}(t_{k+1}, t_k) = \alpha_1 = \mathbf{A}(t_k + \frac{1}{2} \Delta t) \Delta t, \quad (27)$$

which gives rise to the standard, second-order midpoint Magnus propagator (MP2)

$$\mathbf{U}^{[2]}(t_{k+1}, t_k) = \exp[\Omega^{[2]}(t_{k+1}, t_k)]. \quad (28)$$

In contrast, the evaluation of  $\Omega^{[4]}$  requires two grid points, i.e.,  $w_1^{[4]} = \frac{1}{2}$ ,  $c_1^{[4]} = \frac{1}{2} - \frac{\sqrt{3}}{6}$ ,  $w_2^{[4]} = \frac{1}{2}$ , and  $c_2^{[4]} = \frac{1}{2} + \frac{\sqrt{3}}{6}$ , which give rise to

$$\mathbf{Q}^{(2,2)} = \begin{pmatrix} \frac{1}{2} & \frac{1}{2} \\ -\frac{\sqrt{3}}{12} & \frac{\sqrt{3}}{12} \end{pmatrix}, \quad (T^{(2)})^{-1} = \begin{pmatrix} 1 & 0 \\ 0 & 12 \end{pmatrix}, \quad (29)$$

and hence

$$\begin{aligned} \begin{pmatrix} \alpha_1 \\ \alpha_2 \end{pmatrix} &= \Delta t (\mathbf{T}^{(2)})^{-1} \mathbf{Q}^{(2,2)} \begin{pmatrix} \mathbf{A}_1 \\ \mathbf{A}_2 \end{pmatrix} \\ &= \Delta t \begin{pmatrix} \frac{1}{2}(\mathbf{A}_1 + \mathbf{A}_2) \\ \sqrt{3}(\mathbf{A}_2 - \mathbf{A}_1) \end{pmatrix}, \end{aligned} \quad (30)$$

$$\Omega^{[4]}(t_{k+1}, t_k) = \frac{1}{2}(\mathbf{A}_1 + \mathbf{A}_2)\Delta t - \frac{\sqrt{3}}{12}[\mathbf{A}_1, \mathbf{A}_2]\Delta t^2, \quad (31)$$

$$\mathbf{U}^{[4]}(t_{k+1}, t_k) = \exp[\Omega^{[4]}(t_{k+1}, t_k)]. \quad (32)$$

Instead of the above Magnus expansion which involves increasingly nested commutators at high orders, the commutator-free type of expansion of Eq. (13) assumes the following form

$$\mathbf{U}_{\text{CF},m}^{[2s]}(t_{k+1}, t_k) = e^{\tilde{\Omega}} = e^{\tilde{\Omega}_m} e^{\tilde{\Omega}_{m-1}} \cdots e^{\tilde{\Omega}_1}, \quad (33)$$

$$\tilde{\Omega}_i = \sum_{j=1}^s f_{ij} \alpha_j = \Delta t \sum_{k=1}^n x_{ik} \mathbf{A}_k^{[2s]}, \quad x_{ik} = \sum_{j=1}^s f_{ij} g_{jk}, \quad (34)$$

where  $m$  denotes the number of exponentials. The expansion coefficients  $f_{ij}$  can be determined<sup>77</sup> by equating the terms of  $\tilde{\Omega}$  to those of the Magnus expansion  $\Omega$  (14) at each order, up to  $\mathcal{O}(\Delta t^{2s})$ . Consider CFET4 with two exponentials

$$\mathbf{U}_{\text{CF},2}^{[4]}(t_{k+1}, t_k) = e^{f_{21}\alpha_1 + f_{22}\alpha_2} e^{f_{11}\alpha_1 + f_{12}\alpha_2}, \quad (35)$$

where the coefficients should be subject to

$$f_{21} = f_{11}, \quad f_{22} = -f_{12} \quad (36)$$

to fulfill time reversal symmetry. Further use of the Baker-Campbell-Hausdorff formula can be made to merge the two exponentials into one

$$\mathbf{U}_{\text{CF},2}^{[4]}(t_{k+1}, t_k) = e^{2f_{11}\alpha_1 + \frac{f_{12}}{2}[\alpha_1, \alpha_2]}, \quad (37)$$

the exponent of which can be equated to  $\Omega^{[4]}(t_{k+1}, t_k)$  in Eq. (20), thereby leading to (see Algorithm 1)

$$\mathbf{U}_{\text{CF},2}^{[4]}(t_{k+1}, t_k) = e^{\frac{1}{2}\alpha_1 + \frac{1}{6}\alpha_2} e^{\frac{1}{2}\alpha_1 - \frac{1}{6}\alpha_2}. \quad (38)$$

Instead of the termwise matching between CFETn and MPn, the expansion coefficients  $\{f_{ij}\}$  in Eq. (34) can also be optimized<sup>75</sup> to minimize the error between the approximate  $\tilde{\Omega}$  and the exact  $\Omega$ , thereby leading to the optimized (oCFET) variants of CFET. Without going into further details, the required coefficients  $\{x_{ik}\}$  can be determined by reexpressing the coefficients  $\mathbf{A}_n$  defined in equation (25) of Ref. 75 in terms of the present moments  $\mathbf{A}_j^{[2s]}$  (24). The oCFET4 with three exponentials considered here is shown in Algorithm 2.

### 2.3 Predictor-Correctors

The above CFET4 and oCFET4 have to be combined with suitable predictor-correctors to account for the time dependence in RT-TDDFT. The available predictor-correctors<sup>57,72,82,83</sup> were de-

signed only for MP2 and hence cannot be used here. Instead, we got to design new predictor-correctors for CFET4 and oCFET4 case by case.

#### 2.3.1 Predictor-Corrector for CFET4

---

**Algorithm 1** Fourth-order commutator-free exponential time-propagator (CFET4) with two exponentials (equation (43) in Ref. 77)

---

**Subroutine** CFET4( $\mathbf{P}(0)$ ,  $\mathbf{F}(t_1)$ ,  $\mathbf{F}(t_2)$ )

1: **Inputs:**

- 1:  $\mathbf{P}(0)$ ,  $\mathbf{F}(t_1)$ ,  $\mathbf{F}(t_2) \leftarrow t_1 = (\frac{1}{2} - \frac{\sqrt{3}}{6})\Delta t$ ,
- 2:  $t_2 = (\frac{1}{2} + \frac{\sqrt{3}}{6})\Delta t$
- 3:  $\mathbf{U}_1(\Delta t, 0) \leftarrow e^{-i(\frac{3+2\sqrt{3}}{12}\mathbf{F}(t_1) + \frac{3-2\sqrt{3}}{12}\mathbf{F}(t_2))\Delta t}$
- 4:  $\mathbf{U}_2(\Delta t, 0) \leftarrow e^{-i(\frac{3-2\sqrt{3}}{12}\mathbf{F}(t_1) + \frac{3+2\sqrt{3}}{12}\mathbf{F}(t_2))\Delta t}$
- 5:  $\mathbf{P}(\Delta t) \leftarrow \mathbf{U}_2(\Delta t, 0)\mathbf{P}(\Delta t)\mathbf{U}_2^\dagger(\Delta t, 0)$
- 6: **Outputs:**
- 7:  $\mathbf{P}(\Delta t)$

---

As a fourth-order propagator, CFET4 requires two Gauss-Legendre quadrature points. For this reason, an EPEP2 (exponential prediction of density matrix and exponential correction of density matrix at two Gauss-Legendre points) type of predictor-corrector is proposed here, see Algorithm 3 and Fig. 1. The workflow goes as follows.

Step (1): Propagate  $\mathbf{P}(t_k)$  to  $\mathbf{P}(t_1^{[4]})$  with the second-order enforced time reversal symmetry (ETRS) propagator<sup>72</sup> (see Algorithm 4),

$$\mathbf{U}_{\text{ETRS}}(t_{k+1}, t_k) = e^{-i\frac{\Delta t}{2}\mathbf{F}(t_{k+1})} e^{-i\frac{\Delta t}{2}\mathbf{F}(t_k)}, \quad (39)$$

$$\begin{aligned} \mathbf{P}(t_1^{[4]}) &= \mathbf{U}_{\text{ETRS}}(t_{k+1}, t_k) \mathbf{P}(t_k) \mathbf{U}_{\text{ETRS}}^\dagger(t_{k+1}, t_k), \\ t_1^{[4]} &= t_k + c_1^{[4]}\Delta t. \end{aligned} \quad (40)$$

Step (2): Construct  $\mathbf{F}(t_1^{[4]})$  with  $\mathbf{P}(t_1^{[4]})$ .

Step (3): Propagate  $\mathbf{P}(t_1^{[4]})$  to  $\mathbf{P}(t_2^{[4]})$  with Euler's rule,

$$\begin{aligned} \mathbf{P}(t_2^{[4]}) &= e^{-i\mathbf{F}(t_1^{[4]})(t_2^{[4]} - t_1^{[4]})} \mathbf{P}(t_1^{[4]}) e^{i\mathbf{F}(t_1^{[4]})(t_2^{[4]} - t_1^{[4]})}, \\ t_2^{[4]} &= t_k + c_2^{[4]}\Delta t. \end{aligned} \quad (41)$$

Step (4): Construct  $\mathbf{F}(t_2^{[4]})$  with  $\mathbf{P}(t_2^{[4]})$ .

Step (5): Propagate  $\mathbf{P}(t_k)$  to  $\mathbf{P}(t_{k+1})$  with CFET4 (see Algorithm 1).

Step (6): Construct  $\mathbf{F}(t_{k+1})$  with  $\mathbf{P}(t_{k+1})$ .

Step (7): Backward propagate  $\mathbf{P}(t_{k+1})$  to  $\mathbf{P}(t_2^{[4]})$  with Euler's rule,

$$\mathbf{P}(t_2^{[4]}) = e^{i\mathbf{F}(t_{k+1})(t_{k+1} - t_2^{[4]})} \mathbf{P}(t_{k+1}) e^{-i\mathbf{F}(t_{k+1})(t_{k+1} - t_2^{[4]})}, \quad (42)$$

so as to correct  $\mathbf{P}(t_2^{[4]})$ .

Step (8): Repeat steps (4) to (7) until  $\mathbf{P}(t_{k+1})$  converges ac-

cording to the following criterion

$$\frac{\|\mathbf{X}_1 - \mathbf{X}_2\|_F}{M} < \xi, \quad (43)$$

where  $\|\cdot\|_F$  denotes the Frobenius norm,  $\mathbf{X}_1$  and  $\mathbf{X}_2$  represents two  $M \times M$  matrices to be compared, and  $\xi$  is the chosen threshold.

Since  $t_1^{[4]}$  is closer to  $t_k$  than to  $t_{k+1}$  in the above procedure, it is desirable to obtain  $\mathbf{P}(t_1^{[4]})$  from  $\mathbf{P}(t_k)$  rather than from  $\mathbf{P}(t_{k+1})$ . Moreover, since there is no correction to  $\mathbf{P}(t_1^{[4]})$  later on, it is the second-order ETRS instead of the simpler, first-order Euler propagation that has been employed to predict  $\mathbf{P}(t_1^{[4]})$ . The accuracy of  $\mathbf{P}(t_1^{[4]})$  is further furnished by the small time interval  $t_1^{[4]} - t_k$  (which is smaller than the full time interval  $\Delta t$ ).

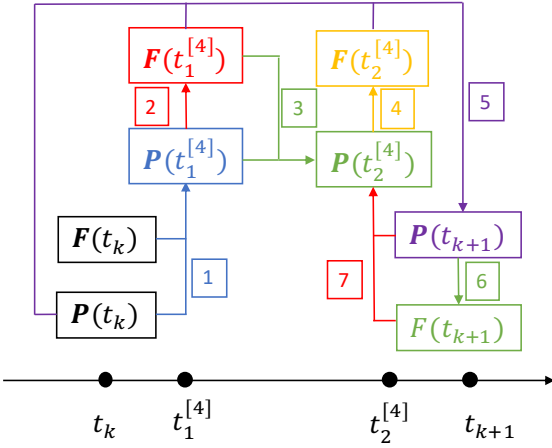


**Fig. 1** One time-step flowchart of EPEP2 for CFET4. In boxes are step indices of Algorithm 3.

### 2.3.2 Predictor-Corrector for oCFET4

Albeit a fourth-order propagator, oCFET4 requires three Gauss-Legendre quadrature points. In the same spirit as EPEP2, an EPEP3 (exponential prediction of density matrix and exponential correction of density matrix at three Gauss-Legendre points) type of predictor-corrector is proposed here, see Algorithm 5 and Fig. 2. The workflows goes as follows.

Step 1: Propagate  $\mathbf{P}(t_k)$  to  $\mathbf{P}(t_1^{[6]})$  with ETRS. Here,  $t_1^{[6]} = t_k + c_1^{[6]} \Delta t$ .

Step 2: Construct  $\mathbf{F}(t_1^{[6]})$  with  $\mathbf{P}(t_1^{[6]})$ .

Step 3: Propagate  $\mathbf{P}(t_1^{[6]})$  to  $\mathbf{P}(t_2^{[6]})$  with Euler's rule,

$$\mathbf{P}(t_2^{[6]}) = e^{-i\mathbf{F}(t_1^{[6]})(t_2^{[6]} - t_1^{[6]})} \mathbf{P}(t_1^{[6]}) e^{i\mathbf{F}(t_1^{[6]})(t_2^{[6]} - t_1^{[6]})},$$

$$t_2^{[6]} = t_k + c_2^{[6]} \Delta t. \quad (44)$$

Step 4: Construct  $\mathbf{F}(t_2^{[6]})$  with  $\mathbf{P}(t_2^{[6]})$ .

Step 5: Propagate  $\mathbf{P}(t_1^{[6]})$  to  $\mathbf{P}(t_3^{[6]})$  with MP2 (28),

$$\mathbf{P}(t_3^{[6]}) = e^{-i\mathbf{F}(t_2^{[6]})(t_3^{[6]} - t_1^{[6]})} \mathbf{P}(t_2^{[6]}) e^{i\mathbf{F}(t_2^{[6]})(t_3^{[6]} - t_1^{[6]})},$$

$$t_3^{[6]} = t_k + c_3^{[6]} \Delta t. \quad (45)$$

**Algorithm 2** Optimized fourth-order commutator-free exponential time-propagator (oCFET4) with three exponentials [see equation (43) in Ref. 75. The coefficients  $x_{ik}$  in Eq. (34) are determined by expressing the coefficients  $\mathbf{A}_n$  defined in equation (25) in Ref. 75 in terms of the matrix moments  $\mathbf{A}_j^{[2s]}$  (24)]

**Subroutine** oCFET4( $\mathbf{P}(0)$ ,  $\mathbf{F}(t_1)$ ,  $\mathbf{F}(t_2)$ ,  $\mathbf{F}(t_3)$ )

1: **Inputs:**

$$\mathbf{P}(0)$$

$$\mathbf{F}(t_1) \leftarrow t_1 = \left(\frac{1}{2} - \frac{\sqrt{15}}{10}\right) \Delta t$$

$$\mathbf{F}(t_2) \leftarrow t_2 = \frac{1}{2} \Delta t$$

$$\mathbf{F}(t_3) \leftarrow t_3 = \left(\frac{1}{2} + \frac{\sqrt{15}}{10}\right) \Delta t$$

$$2: a \leftarrow \begin{pmatrix} \frac{37}{240} - \frac{10\sqrt{15}}{261} & -\frac{1}{30} & \frac{37}{240} + \frac{10\sqrt{15}}{261} \\ -\frac{11}{360} & \frac{23}{45} & -\frac{11}{360} \\ \frac{37}{240} + \frac{10\sqrt{15}}{261} & -\frac{1}{30} & \frac{37}{240} - \frac{10\sqrt{15}}{261} \end{pmatrix}$$

$$3: \mathbf{U}_1(\Delta t, 0) \leftarrow e^{-i\Delta t(a_{31}\mathbf{F}(t_1) + a_{32}\mathbf{F}(t_2) + a_{33}\mathbf{F}(t_3))}$$

$$4: \mathbf{P}(\Delta t) \leftarrow \mathbf{U}_1(\Delta t, 0)\mathbf{P}(0)\mathbf{U}_1^\dagger(\Delta t, 0)$$

$$5: \mathbf{U}_2(\Delta t, 0) \leftarrow e^{-i\Delta t(a_{21}\mathbf{F}(t_1) + a_{22}\mathbf{F}(t_2) + a_{23}\mathbf{F}(t_3))}$$

$$6: \mathbf{P}(\Delta t) \leftarrow \mathbf{U}_2(\Delta t, 0)\mathbf{P}(\Delta t)\mathbf{U}_2^\dagger(\Delta t, 0)$$

$$7: \mathbf{U}_3(\Delta t, 0) \leftarrow e^{-i\Delta t(a_{11}\mathbf{F}(t_1) + a_{12}\mathbf{F}(t_2) + a_{13}\mathbf{F}(t_3))}$$

$$8: \mathbf{P}(\Delta t) \leftarrow \mathbf{U}_3(\Delta t, 0)\mathbf{P}(\Delta t)\mathbf{U}_3^\dagger(\Delta t, 0)$$

9: **Outputs:**

$$\mathbf{P}(\Delta t)$$

**Algorithm 3** Exponential prediction of density matrix and exponential correction of density matrix at two Gauss-Legendre points (EPEP2) for CFET4

1: **Inputs:**

$$\mathbf{P}(0^-) \leftarrow \text{ground state DFT density matrix}$$

$$t_0, t_f, \Delta t$$

$$\tilde{\mathbf{V}}^{(1)} \leftarrow \text{initial perturbation}$$

2: **Initialize:**

$$N \leftarrow (t_f - t_0) / \Delta t$$

$$\mathbf{U}(0^+, 0^-) \leftarrow e^{-i\tilde{\mathbf{V}}^{(1)}}$$

$$\mathbf{P}(0) \equiv \mathbf{P}(0^+) \leftarrow \mathbf{U}(0^+, 0^-)\mathbf{P}(0^-)\mathbf{U}^\dagger(0^+, 0^-)$$

3: **for** step  $k = 0$  to  $N - 1$  **do** ▷ Propagation loop

$$4: t_k \leftarrow k\Delta t$$

$$5: t_a \leftarrow t_k + \left(\frac{1}{2} - \frac{\sqrt{3}}{6}\right) \Delta t$$

$$6: t_b \leftarrow t_k + \left(\frac{1}{2} + \frac{\sqrt{3}}{6}\right) \Delta t$$

$$7: \mathbf{P}_1(t_a) \leftarrow \text{ETRS\_1}(\mathbf{P}(t_k), t_k, t_a) \quad \text{▷ Step 1 (Algorithm 4)}$$

$$8: \mathbf{F}_1(t_a) \leftarrow \text{Fock}(\mathbf{P}_1(t_a)) \quad \text{▷ Step 2}$$

$$9: \mathbf{U}_1(t_b, t_a) \leftarrow e^{-i\mathbf{F}_1(t_a)(t_b - t_a)}$$

$$10: \mathbf{P}_1(t_b) \leftarrow \mathbf{U}_1(t_b, t_a)\mathbf{P}_1(t_a)\mathbf{U}_1^\dagger(t_b, t_a) \quad \text{▷ Step 3}$$

$$11: \mathbf{F}_1(t_b) \leftarrow \text{Fock}(\mathbf{P}_1(t_b)) \quad \text{▷ Step 4}$$

$$12: \mathbf{P}_2(t_{k+1}) \leftarrow \text{CFET4}(\mathbf{P}(t_k), \mathbf{F}_1(t_a), \mathbf{F}_1(t_b)) \quad \text{▷ Step 5}$$

(Algorithm 1)

13: **for** iteration  $i = 2$  to  $N_{\text{it}}$  **do** ▷ Loop until

$$\|\mathbf{P}_{i+1}(t_{k+1}) - \mathbf{P}_i(t_{k+1})\|_F < M\xi$$

$$14: \mathbf{F}_i(t_{k+1}) \leftarrow \text{Fock}(\mathbf{P}_i(t_{k+1})) \quad \text{▷ Step 6}$$

$$15: \mathbf{U}_i(t_b, t_{k+1}) \leftarrow e^{-i\mathbf{F}_i(t_{k+1})(t_{k+1} - t_b)}$$

$$16: \mathbf{P}_i(t_b) \leftarrow \mathbf{U}_i(t_b, t_{k+1})\mathbf{P}_i(t_{k+1})\mathbf{U}_i^\dagger(t_b, t_{k+1}) \quad \text{▷ Step 7}$$

$$17: \mathbf{F}_i(t_b) \leftarrow \text{Fock}(\mathbf{P}_i(t_b)) \quad \text{▷ Step 4}$$

$$18: \mathbf{P}_{i+1}(t_{k+1}) \leftarrow \text{CFET4}(\mathbf{P}(t_k), \mathbf{F}_1(t_a), \mathbf{F}_i(t_b)) \quad \text{▷ Step 5}$$

(Algorithm 1)

19: **end for**

$$20: \mathbf{P}(t_{k+1}) \leftarrow \mathbf{P}_{N_{\text{it}}+1}(t_{k+1})$$

21: **end for**

**Algorithm 4** One-step enforced time reversal symmetry propagator (ETRS, Eq. (39))

**Subroutine** ETRS\_1( $\mathbf{P}(t_0)$ ,  $t_0$ ,  $t_1$ )

```

1: Inputs:
   $\mathbf{P}(t_0)$ ,  $t_0$ ,  $t_1$ 
2:  $\Delta t \leftarrow t_1 - t_0$ 
3:  $\mathbf{F}(t_0) \leftarrow \text{Fock}(\mathbf{P}(t_0))$ 
4:  $\mathbf{U}_0(t_0 + \frac{\Delta t}{2}, t_0) \leftarrow e^{-i\mathbf{F}(t_0)\frac{\Delta t}{2}}$ 
5:  $\mathbf{P}_1(t_0 + \frac{\Delta t}{2}) \leftarrow \mathbf{U}_0(t_0 + \frac{\Delta t}{2}, t_0)\mathbf{P}(t_0)\mathbf{U}_0^\dagger(t_0 + \frac{\Delta t}{2}, t_0)$  ▷ Step 1
6:  $\mathbf{U}_1(t_1, t_0) \leftarrow e^{-i\mathbf{F}_1(t_0)\Delta t}$ 
7:  $\mathbf{P}_2(t_1) \leftarrow \mathbf{U}_1(t_1, t_0)\mathbf{P}(t_0)\mathbf{U}_1^\dagger(t_1, t_0)$  ▷ Step 2
8: for iteration  $i = 2$  to  $N_{\text{it}}$  do ▷ Loop until
    $\|\mathbf{P}_{i+1}(t_{k+1}) - \mathbf{P}_i(t_{k+1})\|_F < M\xi$ 
9:    $\mathbf{F}_i(t_1) \leftarrow \text{Fock}(\mathbf{P}_i(t_1))$  ▷ Step 3
10:   $\mathbf{U}_i(t_1, t_0 + \frac{\Delta t}{2}) \leftarrow e^{-i\mathbf{F}_i(t_1)\frac{\Delta t}{2}}$ 
11:   $\mathbf{P}_{i+1}(t_1) \leftarrow \mathbf{U}_i(t_1, t_0 + \frac{\Delta t}{2})\mathbf{P}(t_0 + \frac{\Delta t}{2})\mathbf{U}_i^\dagger(t_1, t_0 + \frac{\Delta t}{2})$  ▷ Step 4
12: end for
13: Outputs:
   $\mathbf{P}_{N_{\text{it}}+1}(t_1)$ 

```

Step 6: Construct  $\mathbf{F}(t_3^{[6]})$  with  $\mathbf{P}(t_3^{[6]})$ .

Step 7: Propagate  $\mathbf{P}(t_k)$  to  $\mathbf{P}(t_{k+1})$  with oCFET4 (see Algorithm 2).

Step 8: Construct  $\mathbf{F}(t_{k+1})$  with  $\mathbf{P}(t_{k+1})$ .

Step 9: Backward propagate  $\mathbf{P}(t_{k+1})$  to  $\mathbf{P}(t_3^{[6]})$  with Euler's rule,

$$\mathbf{P}(t_3^{[6]}) = e^{i\mathbf{F}(t_{k+1})(t_{k+1} - t_3^{[6]})} \mathbf{P}(t_{k+1}) e^{-i\mathbf{F}(t_{k+1})(t_{k+1} - t_3^{[6]})}, \quad (46)$$

so as to correct  $\mathbf{P}(t_3^{[6]})$ .

Step 10: Construct  $\mathbf{F}(t_3^{[6]})$  with  $\mathbf{P}(t_3^{[6]})$ .

Step 11: Backward propagate  $\mathbf{P}(t_3^{[6]})$  to  $\mathbf{P}(t_4)$  with Euler's rule,

$$\mathbf{P}(t_4) = e^{i\mathbf{F}(t_3^{[6]})(t_3^{[6]} - t_4)} \mathbf{P}(t_3^{[6]}) e^{-i\mathbf{F}(t_3^{[6]})(t_3^{[6]} - t_4)},$$

$$t_4 = \frac{t_2^{[6]} + t_3^{[6]}}{2}. \quad (47)$$

Step 12: Construct  $\mathbf{F}(t_4)$  with  $\mathbf{P}(t_4)$ .

Step 13: Backward propagate  $\mathbf{P}(t_3^{[6]})$  to  $\mathbf{P}(t_2^{[6]})$  with MP2 (28),

$$\mathbf{P}(t_2^{[6]}) = e^{i\mathbf{F}(t_4)(t_3^{[6]} - t_2^{[6]})} \mathbf{P}(t_3^{[6]}) e^{-i\mathbf{F}(t_4)(t_3^{[6]} - t_2^{[6]})}, \quad (48)$$

so as to correct  $\mathbf{P}(t_2^{[6]})$ .

Step 14: Construct  $\mathbf{F}(t_2^{[6]})$  with  $\mathbf{P}(t_2^{[6]})$ .

Step 15: Repeat steps (7) to (14) until  $\mathbf{P}(t_{k+1})$  converges according to criterion (43).

In the above procedure,  $\mathbf{P}(t_1^{[6]})$  is predicted from  $\mathbf{P}(t_k)$  by using ETRS and is not further corrected by  $\mathbf{P}(t_{k+1})$ . This follows the same argument as in EPEP2 and is because the time moment  $t_1^{[6]}$  is much closer to  $t_k$  than to  $t_{k+1}$ .  $\mathbf{P}(t_3^{[6]})$  is corrected by using the backward Euler propagation of  $\mathbf{P}(t_{k+1})$ , for  $t_3^{[6]}$  is closer to

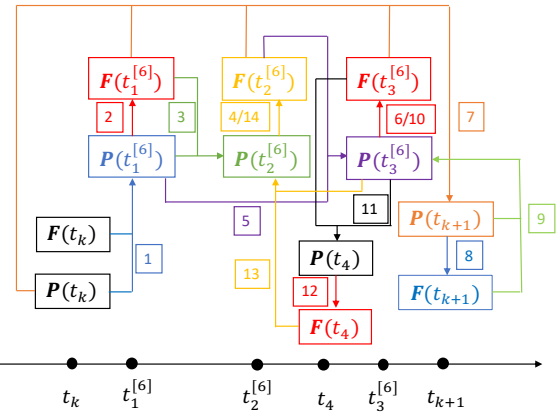


**Fig. 2** One time-step flowchart of EPEP3 for oCFET4. In boxes are step indices of Algorithm 5.

$t_{k+1}$ . Since the interval  $t_3^{[6]} - t_2^{[6]}$  for  $\mathbf{P}(t_2^{[6]})$  is larger than the interval  $t_{k+1} - t_3^{[6]}$  for  $\mathbf{P}(t_3^{[6]})$ , an auxiliary time moment  $t_4$  has been introduced to correct  $\mathbf{P}(t_2^{[6]})$  by using the backward MP2 propagation from  $\mathbf{P}(t_3^{[6]})$ .

## 2.4 Time Step

Having chosen an appropriate propagator (e.g., MP2 for low-lying valence excitations and oCFET4 for core excitations), along with the corresponding corrector-predictor, the next step is to choose an appropriate time step  $\Delta t$ . It is well known that  $\Delta t$  is bounded by both the stability and accuracy of the chosen propagator as well as the Nyquist criterion for signal sampling<sup>84,85</sup>, i.e.,  $\Delta t \leq \Delta t_H = \frac{1}{f_s} < \frac{1}{2f_H}$ , with  $f_H$  being the highest frequency contained in the sampled signal. Literally, the sampling frequency  $f_s$  ( $= 1/\Delta t$ ) must be twice larger than the width  $f_H - (-f_H)$  of the spectrum contained in the band limited real signal. This restriction is to avoid the so-called aliasing phenomenon, which stems from the fact that every frequency within  $[-f_H, f_H]$  will be copied infinitely many times (separated by the sampling frequency  $f_s$ ) by the Fourier transform of the sampled signal. However, if the spectrum  $[-f_H, f_H]$  is separated in blocks and only one particular block is of interest, an even larger time step  $\Delta t$  can be chosen to sample the signal. To see this, consider the spectrum of a real-valued time signal shown in Fig. 3, which has four blocks,  $[-f_H, -f_L]$ ,  $[-B, 0]$ ,  $[0, B]$ , and  $[f_L, f_H]$ . To extract the frequencies within  $[0, B]$ , the proper sampling frequency  $f_s$  can be determined by the requirement that no alias from the other blocks will appear in the interval  $[0, B]$ . Consider first the block  $[f_L, f_H]$ , which is shifted to the left by  $(n - 1)$  times until the right end of  $[0, B]$ . The next left shift of  $[f_L, f_H]$  must cross  $[0, B]$  in one step of  $f_s$ , thereby resulting in the first necessary condition for  $f_s$ ,

$$f_s > B + f_H - f_L. \quad (49)$$

The same is obtained by right shifts of  $[-f_H, -f_L]$  in steps of  $f_s$ . Likewise, the one-step right shift of  $[-B, 0]$  gives rise to the following necessary condition

$$f_s > 2B. \quad (50)$$

**Algorithm 5** Exponential prediction of density matrix and exponential correction of density matrix at three Gauss-Legendre points (EPEP3) for the oCFET4 propagator.

---

1: **Inputs:**

- $\mathbf{P}(0^-) \leftarrow$  ground state DFT density matrix
- $t_0, t_f, \Delta t$
- $\tilde{\mathbf{V}}^{(1)} \leftarrow$  initial perturbation

2: **Initialize:**

- $N \leftarrow (t_f - t_0) / \Delta t$
- $\mathbf{U}(0^+, 0^-) \leftarrow e^{-i\tilde{\mathbf{V}}^{(1)}}$
- $\mathbf{P}(0) \equiv \mathbf{P}(0^+) \leftarrow \mathbf{U}(0^+, 0^-) \mathbf{P}(0^-) \mathbf{U}^\dagger(0^+, 0^-)$

3: **for** step  $k = 0$  to  $N - 1$  **do** ▷ Propagation loop

- 4:  $t_k \leftarrow k\Delta t$
- 5:  $t_a \leftarrow t_k + (\frac{1}{2} - \frac{\sqrt{15}}{10})\Delta t$
- 6:  $t_b \leftarrow t_k + \frac{1}{2}\Delta t$
- 7:  $t_c \leftarrow t_k + (\frac{1}{2} + \frac{\sqrt{15}}{10})\Delta t$
- 8:  $t_d \leftarrow \frac{t_b + t_c}{2}$
- 9:  $\mathbf{P}_1(t_a) \leftarrow \text{ETRS\_1}(\mathbf{P}(t_k), t_k, t_a)$  ▷ Step 1 (Algorithm 4)
- 10:  $\mathbf{F}_1(t_a) \leftarrow \text{Fock}(\mathbf{P}_1(t_a))$  ▷ Step 2
- 11:  $\mathbf{U}_1(t_b, t_a) \leftarrow e^{-i\mathbf{F}_1(t_a)(t_b - t_a)}$  ▷ Step 3
- 12:  $\mathbf{P}_1(t_b) \leftarrow \mathbf{U}_1(t_b, t_a) \mathbf{P}_1(t_a) \mathbf{U}_1^\dagger(t_b, t_a)$  ▷ Step 4
- 13:  $\mathbf{F}_1(t_b) \leftarrow \text{Fock}(\mathbf{P}_1(t_b))$  ▷ Step 5
- 14:  $\mathbf{U}_1(t_c, t_a) \leftarrow e^{-i\mathbf{F}_1(t_b)(t_c - t_a)}$  ▷ Step 6
- 15:  $\mathbf{P}_1(t_c) \leftarrow \mathbf{U}_1(t_c, t_a) \mathbf{P}_1(t_a) \mathbf{U}_1^\dagger(t_c, t_a)$  ▷ Step 7
- 16:  $\mathbf{F}_1(t_c) \leftarrow \text{Fock}(\mathbf{P}_1(t_c))$  ▷ Step 8
- 17:  $\mathbf{P}_2(t_{k+1}) \leftarrow \text{oCFET4}(\mathbf{P}(t_k), \mathbf{F}_1(t_a), \mathbf{F}_1(t_b), \mathbf{F}_1(t_c))$  ▷ Step 9

(Algorithm 2)

18: **for** iteration  $i = 2$  to  $N_{\text{it}}$  **do** ▷ Loop until

- 19:  $\|\mathbf{P}_{i+1}(t_{k+1}) - \mathbf{P}_i(t_{k+1})\|_F < M\xi$  ▷ Step 10
- 20:  $\mathbf{F}_i(t_{k+1}) \leftarrow \text{Fock}(\mathbf{P}_i(t_{k+1}))$  ▷ Step 11
- 21:  $\mathbf{U}_i(t_c, t_{k+1}) \leftarrow e^{i\mathbf{F}_i(t_{k+1})(t_{k+1} - t_c)}$  ▷ Step 12
- 22:  $\mathbf{P}_i(t_c) \leftarrow \mathbf{U}_i(t_c, t_{k+1}) \mathbf{P}_i(t_{k+1}) \mathbf{U}_i^\dagger(t_c, t_{k+1})$  ▷ Step 13
- 23:  $\mathbf{F}_i(t_c) \leftarrow \text{Fock}(\mathbf{P}_i(t_c))$  ▷ Step 14
- 24:  $\mathbf{U}_i(t_d, t_c) \leftarrow e^{i\mathbf{F}_i(t_c)(t_d - t_c)}$  ▷ Step 15
- 25:  $\mathbf{P}_i(t_d) \leftarrow \mathbf{U}_i(t_d, t_c) \mathbf{P}_i(t_c) \mathbf{U}_i^\dagger(t_d, t_c)$  ▷ Step 16
- 26:  $\mathbf{F}_i(t_d) \leftarrow \text{Fock}(\mathbf{P}_i(t_d))$  ▷ Step 17
- 27:  $\mathbf{U}_i(t_b, t_c) \leftarrow e^{i\mathbf{F}_i(t_d)(t_b - t_c)}$  ▷ Step 18
- 28:  $\mathbf{P}_i(t_b) \leftarrow \mathbf{U}_i(t_b, t_c) \mathbf{P}_i(t_c) \mathbf{U}_i^\dagger(t_b, t_c)$  ▷ Step 19
- 29:  $\mathbf{F}_i(t_b) \leftarrow \text{Fock}(\mathbf{P}_i(t_b))$  ▷ Step 20
- 30:  $\mathbf{P}_{i+1}(t_{k+1}) \leftarrow \text{oCFET4}(\mathbf{P}(t_k), \mathbf{F}_1(t_a), \mathbf{F}_i(t_b), \mathbf{F}_i(t_c))$  ▷ Step 21

Step 7 (Algorithm 2)

31: **end for**

32: **end for**

---

The two conditions (49) and (50) can be combined to yield the lower bound  $\tilde{f}_s$  of  $f_s$

$$\tilde{f}_s = \max\{B + f_H - f_L, 2B\} < f_s. \quad (51)$$

Moreover, it is obvious that the following conditions

$$f_L - (n - 1)f_s > B, \quad f_H - nf_s < 0, \quad n = 1, 2, \dots, \quad (52)$$

should also be satisfied simultaneously for the left shifts of  $[f_L, f_H]$ . The conditions in Eqs. (51) and (52) can be combined to yield

$$\frac{f_H}{n} < f_s < \frac{f_L - B}{n - 1}, \quad 1 \leq n \leq \left\lfloor \frac{f_L - B}{\tilde{f}_s} \right\rfloor + 1, \quad (53)$$

where the symbol  $\lfloor y \rfloor$  denotes the largest integer less than or equal to  $y$ . Similarly, the following conditions

$$-f_L + (m - 1)f_s < 0, \quad -f_H + mf_s > B, \quad m = 1, 2, \dots, \quad (54)$$

should be satisfied additionally for the right shifts of  $[-f_H, -f_L]$ . The conditions in Eqs. (51) and (54) can be combined to yield

$$\frac{f_H + B}{m} < f_s < \frac{f_L}{m - 1}, \quad 1 \leq m \leq \left\lfloor \frac{f_L}{\tilde{f}_s} \right\rfloor + 1. \quad (55)$$

Finally, no additional condition is required for the right shift of  $[-B, 0]$ .

In summary, to read out correctly the frequencies in the interval  $[0, B]$  from the Fourier transform of the sampled signal, the sampling frequency  $f_s$  has to satisfy conditions in Eqs. (51), (53), and (55) simultaneously. The analysis can readily be generalized to extract the frequencies of any block of a spectrum composed of  $2N$  blocks. The algorithm goes as follows.

- (1) Calculate the energy differences  $\epsilon_a - \epsilon_i$  between the ground-state unoccupied and occupied canonical molecular orbitals (CMO), and sort them in ascending order  $\{\Delta\epsilon_n\}_{n=1}^{N_o N_v}$ .
- (2) Partition  $\{\Delta\epsilon_n\}_{n=1}^{N_o N_v}$  into blocks. If the separation between  $\Delta\epsilon_n$  and  $\Delta\epsilon_{n+1}$  is larger than  $\omega_C = 2\omega_b + \omega_c$ , set  $\Delta\epsilon_n$  and  $\Delta\epsilon_{n+1}$  as the uppermost and lowermost elements of the current and next blocks, respectively. Here,  $\omega_b$  is a parameter (e.g., 0.5 a.u.) to broaden each block, so as to account for the uncertainties of the independent particle approximation (IPA) of the true excitation energies, whereas  $\omega_c$  is another parameter (e.g., 0.2 a.u.) to ensure the minimal separation between two adjacent broadened blocks. The in total  $N$  blocks  $[f_{Li}, f_{Hi}]_{i=1}^N$  along with their negative counter parts  $[-f_{Hi}, -f_{Li}]_{i=1}^N$  form the estimated structure of the whole TDKS spectrum.
- (3) Choose a target block, say  $[f_{Lk}, f_{Hk}]$ , and calculate the minimal sampling frequency

$$\tilde{f}_s = f_{Hk} - f_{Lk} + \max_{i \in [1, N]} (f_{Hi} - f_{Li}). \quad (56)$$

- (4) Build up the corresponding inequalities for each block  $[f_a, f_b]$  ( $f_b > f_a$ ; including those of negative frequencies). For those

blocks lower and higher than  $[f_{Lk}, f_{Hk}]$ , we have

$$\frac{f_{Hk} - f_a}{n} < f_s < \frac{f_{Lk} - f_b}{n-1}, \quad 1 \leq n \leq \left\lfloor \frac{f_{Lk} - f_b}{\tilde{f}_s} \right\rfloor + 1, \quad (57)$$

and

$$\frac{f_b - f_{Lk}}{n} < f_s < \frac{f_a - f_{Hk}}{n-1}, \quad 1 \leq n \leq \left\lfloor \frac{f_a - f_{Hk}}{\tilde{f}_s} \right\rfloor + 1, \quad (58)$$

respectively.

(5) Determine the intersection of the inequalities of all blocks so as to obtain the allowed sampling frequency  $f_s$  and hence the time step  $\Delta t = 1/f_s$ .

Note that when the whole spectrum is regarded as one big block  $[-f_H, f_H]$ , the above algorithm reduces naturally to the Nyquist time step  $\Delta t_H = \frac{1}{f_s} = \frac{1}{2f_H}$ , as can be seen from Eq. (56).

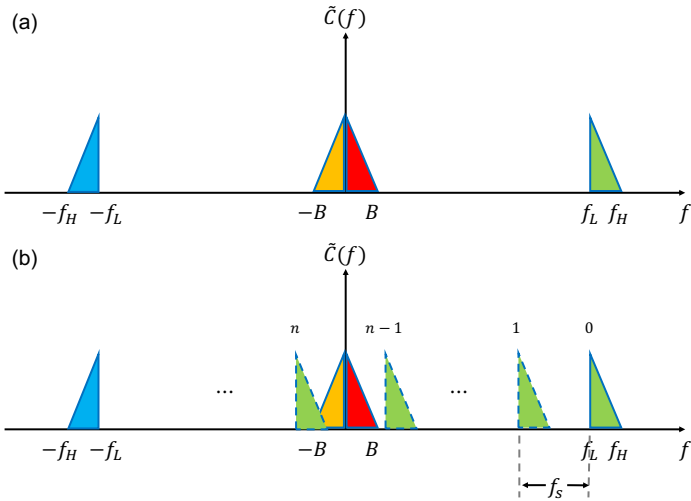


**Fig. 3** (a) Schematic representation of a sparse spectrum, with frequencies located in blocks  $[-f_H, -f_L]$ ,  $[-B, 0]$ ,  $[0, B]$ , and  $[f_L, f_H]$ . (b) Green blocks with dashed contour lines are periodic images (aliases) of the original frequencies in  $[f_L, f_H]$ , separated by the sampling frequency  $f_s$ . The conditions in Eq. (53) ensure that the  $n$ -th and  $(n-1)$ -th image blocks of  $[f_L, f_H]$  are located on the left and right hands of sides of  $[0, B]$ , respectively. Further incorporation of the conditions in Eq. (55) will separate the  $n$ -th image block of  $[f_L, f_H]$  from  $[-B, 0]$ , as a result of the separation between  $[0, B]$  and the  $n$ -th image block of  $[-f_H, -f_L]$  (because  $[-f_H, -f_L]$  and  $[f_L, f_H]$  are symmetric with respect to the 0 Hz axis).

At this stage, it must be realized that the time step determined by the above algorithm only guarantees that the target frequencies are not messed up with aliases from the other blocks. The accuracy of the spectral analysis depends further on the quality of the input time signal. For a given propagator, the smaller the time step, the more accurate the time signal. On the other hand, for a given time step, the more accurate the propagator, the more accurate the time signal. However, a very small time step or a very accurate propagator usually implies a very high computational cost. Therefore, it is important to balance these factors in the allowed range of sampling frequency. To achieve this, we first

tried to use the following parameter

$$\tau_P = \frac{\|\mathbf{P}(t) - \mathbf{P}_{\text{ref}}(t)\|_F}{M \cdot t} \quad (59)$$

to quantify the accuracy of  $\mathbf{P}(t)$  (evolved by the chosen propagator with time step  $\Delta t$ ) against a reference 1PDM  $\mathbf{P}_{\text{ref}}(t)$  (obtained by CF6:5Opt (see Table 6 in Ref. 75) with  $\Delta t_H/2$ ). However, preliminary experimentation reveals that, for core excitations,  $\tau_P$  is rather sensitive to all the ingredients (atomic number, XC functional, electron kinematics, and basis set), meaning that it is not directly connected to the target accuracy. Having realized that such ingredients have been ‘renormalized’ into the lowest core level  $\epsilon_{1s}$  of the ground-state calculation, we switch to seek for a relation between  $\Delta t$  and  $\epsilon_{1s}$  for core excitations. As can be seen from Fig. 4 and Table 1, for the  $K$ -edge core excitations of HX (X = F, Cl, Br), there exist very good linear relations between  $\log_{10}(\Delta t)$  and  $\log_{10}(|\epsilon_{1s}|)$  for both CFET4 and oCFET4. It is just that the slopes and interceptions are slightly different for different XC functionals (because different functionals leads to different degrees of noncommutativity between KS matrices at different times, the more exact exchange, the more enhanced noncommutativity). Although such relations have been obtained based on nonrelativistic calculations with a single basis set, they should be applicable to other basis sets and other systems with relativistic effects accounted for. The underlying reasons are twofold: (1) different basis sets produce essentially the same energies for all the occupied and low-lying virtual orbitals and (2) relativity is heavily dominated by the time-independent one-body terms (which do not cause noncommutativity between KS matrices at different times). In other words, such linear relations are very robust with respect to atomic number, electron kinematics, and basis set, and can hence be applied to all the elements in the Periodic Table, to achieve a better than 0.05 eV accuracy for core excitation energies as compared to those by LR-TDDFT. To confirm this, the predicted time step will be taken in Sec. 3 for the  $K$ - and  $L$ -edge excitations of HI. Note in passing that the time step predicted by the linear relations should further be verified to comply with the above alias-free conditions. If not, it should be reduced to the largest allowed value.

After having determined the time step for each propagator, it is attempting to know which propagator will be most efficient in terms of the number of Fock matrix builds. To this end, the numbers ( $N_{\text{FBS}}$ ) of Fock builds per time step are summarized in Table 2 for MP2, CFET4, and oCFET4. Since the total sampling time  $T$  is determined by the spectral resolution, it is the same for all propagators. Therefore, the relative efficiency of two propagators can be measured by the ratio between their  $N_{\text{FBS}}/\Delta t$  values, the smaller, the more efficient.

Finally, given the time series  $\{\mathbf{P}_\beta(t_n)\}_{n=0}^{N-1}$  ( $t_n = n\Delta t$ ) of 1PDM, induced by an external field along a direction  $\beta \in \{x, y, z\}$ , one can calculate many interesting quantities such as the induced electric dipole moment tensor

$$\mu_{\alpha\beta}^{\text{ind}}(t_n) = -\text{Tr}[\tilde{\mathbf{V}}_\alpha \mathbf{P}_\beta(t_n)] + \text{Tr}[\tilde{\mathbf{V}}_\alpha \mathbf{P}^{(0)}(0^-)], \quad n \in [0, N-1], \quad (60)$$

which can further be transformed<sup>86–88</sup> to the frequency domain

to obtain the electric dynamical dipole polarizability

$$\alpha_{\alpha\beta}(\omega) = \frac{1}{\kappa} \mu_{\alpha\beta}^{\text{ind}}(\omega), \quad (61)$$

and hence the absorption spectrum (dipole strength function)

$$S(\omega) = \frac{4\pi\omega}{3c} \Im \text{Tr} \alpha(\omega). \quad (62)$$

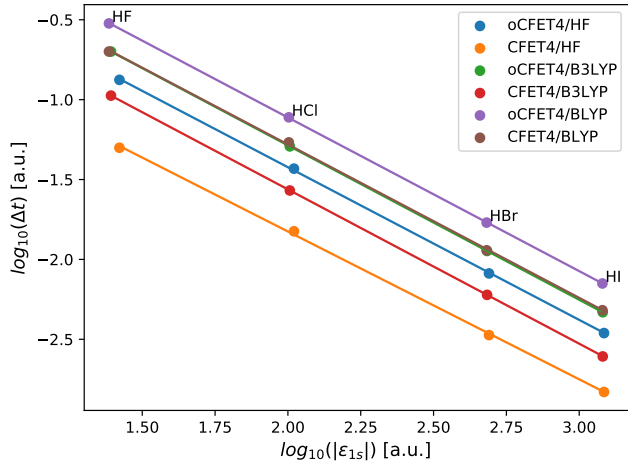


**Fig. 4** Linear relations between  $\log_{10}(\Delta t)$  and  $\log_{10}(|\epsilon_{1s}|)$  for  $K$ -edge core excitations of HF, HCl, and HBr by CFET4@RT-TDDFT and oCFET4@RT-TDDFT with different exchange-correlation functionals.

**Table 1** Fitting functions  $\log_{10}(\Delta t) = a \cdot \log_{10}(|\epsilon_{1s}|) + b$  for  $K$ -edge core excitations by CFET4@RT-TDDFT and oCFET4@RT-TDDFT (cf. Fig. 4)

propagator	functional	$a$	$b$
CFET4	HF	-0.92526295	0.02526600
	B3LYP	-0.96592829	0.37019600
	BLYP	-0.96018601	0.63991532
oCFET4	HF	-0.95558724	0.48821463
	B3LYP	-0.96656731	0.64711096
	BLYP	-0.96171191	0.81185106

**Table 2** The numbers ( $N_{\text{FBS}}$ ) of Fock matrix builds per time step involved in the predictor-correctors

Predictor-Corrector	Propagator	$N_{\text{FBS}}^a$	Formal order
EPPC <sup>b</sup>	MP2	$N_{\text{it}}$	2
EPEP2 <sup>c</sup>	CFET4	$3 \cdot N_{\text{it}}$	4
EPEP3 <sup>d</sup>	oCFET4	$5 \cdot N_{\text{it}} - 1$	4

<sup>a</sup>  $N_{\text{it}}$ : average number of iterations in each *for* loop within a time step.

<sup>b</sup> Algorithm 2 in Ref. 83.

<sup>c</sup> Algorithm 3.

<sup>d</sup> Algorithm 5.

### 3 Pilot Applications

To illustrate the usefulness of the  $\log_{10}(\Delta t)$ - $\log_{10}(|\epsilon_{1s}|)$  relations (see Table 1) for core excitations by CFET4/oCFET4@RT-TDDFT, the HI molecule is taken here as a showcase. The spin-free (sf) part<sup>89,90</sup> of the exact two-component (X2C) Hamiltonian<sup>91,92</sup>, the HF, B3LYP<sup>93,94</sup>, and BLYP<sup>95,96</sup> XC functionals, and the JORGE-ADZP basis set<sup>97</sup> are used in all calculations with the BDF program package<sup>98–101</sup>. The interatomic distance of HI is optimized to be 1.542/1.559/1.571 Å at the sfX2C-HF/B3LYP/BLYP level. Given the energy  $\epsilon_{1s}$  of the lowest occupied orbital, the time step  $\Delta t$  for each propagator and XC functional is first predicted by the  $\log_{10}(\Delta t)$ - $\log_{10}(|\epsilon_{1s}|)$  linear relation. If it does not comply with the alias-free conditions (which involve only the ground-state orbital energies; cf. Sec. 2.4), it will be reduced to the largest allowed value. The so-determined time steps are documented in Table 3. The total simulation time is another parameter that needs to be estimated in advance. In the present simulations, it is first estimated according to the “informational uncertainty principle”<sup>87</sup>, i.e.,  $T \sim \frac{4\pi}{\delta\bar{\omega}}$ , with  $\bar{\omega}$  being the average separation between core excitation energies estimated by IPA, that is,  $\bar{\omega}$  is just the average separation between the low-lying unoccupied CMOs. Note that virtual CMOs higher than 300 a.u. are excluded in the dynamics simulations, for they do not affect the excitation energies reported here (by less 1 meV).

To facilitate the dynamics simulation as well as state assignment, the full molecular symmetry should be used. For HI, the  $A_1$  irreducible representation (irrep) of  $C_{\infty v}$  can be used to obtain  $A_1$  type of excited states if the applied electric field is along the  $z$  (bonding) direction, whereas the  $E_1$  irrep of  $C_{\infty v}$  should be used to obtain  $E_1$  type of excited states if the applied electric field is along both the  $x$  and  $y$  directions. For the latter, it is operationally much simpler to work with  $C_s$ , which is the highest subgroup of  $C_{\infty v}$ , where  $x$  (or  $y$ ) transforms as the totally symmetric irrep (i.e.,  $C_s(\sigma_y)$  for  $x$  and  $C_s(\sigma_x)$  for  $y$ ). Since  $x^2$  and  $y^2$  can be rotated to each other,  $\alpha_{xx}(\omega)$  is strictly identical with  $\alpha_{yy}(\omega)$ , such that only one of the  $x$  and  $y$  directions needs to be considered to obtain both  $\alpha_{xx}(\omega)$  and  $\alpha_{yy}(\omega)$ . Nevertheless, only the reflection-symmetric component of a  $E_1$  state can be obtained in this case. Note in passing that it is a must instead of merely a trick to use  $C_s$  if the applied  $x$ - or  $y$ -field is very strong. In that case, both  $A_1$  and  $E_n$  ( $n \geq 2$ ) types of excited states can also be obtained, resulting from the reflection-symmetric decompositions of  $E_1^\beta \otimes E_1^\beta \cdots \otimes E_1^\beta$ ,  $\beta \in \{x, y\}$ . In contrast, the  $A_2$  type of excited states still cannot be obtained, unless the angular momentum  $l_z$  is used in place of the electric dipole moment.

Among all things, the stability of a dynamics simulation should first be checked. As can be seen from Fig. 5, the energy conservation errors  $E(t_{k+1}) - E(t_k)$  are very small for both CFET4@RT-TDDFT/HF and oCFET4@RT-TDDFT/HF. Although not documented here, such errors are even smaller for the B3LYP and BLYP functionals.

The  $K$ - and  $L$ -edge absorption spectra of HI, obtained by the FD analyses of the CFET4@RT-TDDFT/HF and oCFET4@RT-TDDFT/HF signals, are plotted in Figs. 6 and 7, respectively, which are in good agreement with those by LR-TDDFT/HF, where

**Table 3** Time steps ( $\Delta t$ ) of CFET4/oCFET4@RT-TDDFT (MP2@RT-TDDFT) for core (valence) excitations of HI

excitation	functional	$\Delta t/\text{a.u.}$ CFET4	$\Delta t/\text{a.u.}$ oCFET4	$\Delta t/\text{a.u.}$ MP2	$T/\text{a.u.}^*$
core	HF	0.00148	0.00346	385 (320)	
	B3LYP	0.00247	0.00440	455 (480)	
	BLYP	0.00481	0.00707	417 (400)	
valence	HF			0.0507	407 (700)

\* Simulation time estimated according to  $\frac{4\pi}{\delta\omega}$ , with  $\bar{\omega}$  being the average separation between core/valence excitation energies estimated by IPA. In parentheses are the actually needed simulation time to just resolve the spectra.

the fully symmetrized<sup>66</sup> iVI approach<sup>67,68</sup> is employed to obtain directly those roots belonging to a given energy window, without knowing in advance the number or characters of the roots. To make the comparison even sharper, the  $K$ - and  $L$ -edge excitation energies of HI are further given in Tables 4 and 5, respectively. It can be seen that, for all the considered functionals, the deviations of CFET4/oCFET4@RT-TDDFT from LR-TDDFT are all below 0.05 eV, which is just the tolerance when training the  $\log_{10}(\Delta t)$ - $\log_{10}(|\epsilon_{1s}|)$  linear relations with respect to the  $K$ -edge excitations of HX (X = F, Cl, Br). As such, the robustness of these relations is fully confirmed.

As far as computational efficiency is concerned, the relative efficiency of oCFET4@RT-TDDFT and CFET4@RT-TDDFT can readily be estimated by the ratio between their  $N_{\text{FBS}}/\Delta t$  values (cf. Tables 2 and 3). Since both propagators requires two cycles at each time step to converge the corresponding implicit predictor-correctors (EPEP3 vs EPEP2), it can readily checked that oCFET@RT-TDDFT is a bit more efficient than CFET@RT-TDDFT for the HF and B3LYP functionals, by 36% and 16%, respectively. That is, the computational overhead of oCFET@RT-TDDFT over CFET@RT-TDDFT per time step is compensated for by its larger time step and hence fewer number of steps. Nevertheless, the two propagators are computationally very much the same for the BLYP functional.

For low-lying valence excitations, MP2 (28) in conjunction with the implicit EPPC predictor-corrector<sup>83</sup> is usually accurate enough, and is generally more efficient than higher-order propagators such as oCFET and CFET. The time step is chosen here to be the largest alias-free value (cf. Table 3 and Sec. 2.4). As can be seen from Table 6, MP2@RT-TDDFT does perform very well for the low-lying valence excitations of HI.

## 4 Conclusion

A robust AutoPST approach has been proposed to run relativistic RT-TDDFT simulations of core excitation spectra of systems composed of any elements in the Periodic Table. It is composed of the following ingredients: (1) the just good enough and most efficient propagator oCFET4<sup>75</sup> along with the EPEP3 predictor-corrector, (2) very robust linear relations and alias-free conditions for determining automatically the largest possible time steps, and (3) *a priori* estimates of the total simulation times. Although only scalar relativity has been taken into account in the pilot applications, AutoPST should work well also for fully relativistic RT-

**Table 4** Deviations ( $\Delta\Delta E$  in eV) of CFET4@RT-TDDFT and oCFET4@RT-TDDFT from LR-TDDFT ( $\Delta E$  in eV) for the  $K$ -edge core excitations of HI\*

functional	term	$\Delta E$	oscillator strength	$\Delta\Delta E$ (CFET4)	$\Delta\Delta E$ (oCFET4)
HF	$A_1(\Sigma^+)$	33098.70	0.0001	0.04	0.04
	$A_1(\Sigma^+)$	33102.40	0.0000	0.03	0.03
	$E_1(\Pi)$	33104.04	0.0000	0.02	0.02
	$A_1(\Sigma^+)$	33104.24	0.0000	0.02	0.02
	$E_1(\Pi)$	33104.72	0.0000	0.02	0.03
	$E_2(\Lambda)$	33105.17	0.0000	0.03	0.03
	$A_1(\Sigma^+)$	32771.97	0.0001	0.05	0.03
	$A_1(\Sigma^+)$	32774.02	0.0000	0.03	0.02
	$A_1(\Sigma^+)$	32775.01	0.0000	0.02	0.02
	$E_1(\Pi)$	32775.46	0.0001	0.03	0.02
B3LYP	$E_1(\Pi)$	32776.23	0.0000	0.04	0.02
	$A_1(\Sigma^+)$	32776.49	0.0000	0.02	0.02
	$A_1(\Sigma^+)$	32693.99	0.0000	-0.01	-0.01
	$A_1(\Sigma^+)$	32695.68	0.0001	0.00	0.00
	$A_1(\Sigma^+)$	32696.54	0.0000	0.00	0.00
	$E_1(\Pi)$	32697.03	0.0004	0.00	0.00
	$E_1(\Pi)$	32697.96	0.0000	0.00	0.00
	$A_1(\Sigma^+)$	32698.01	0.0001	0.00	0.00

\* The  $E_2$  state can only be obtained by adding a constant perturbation to the electric field (see the text).

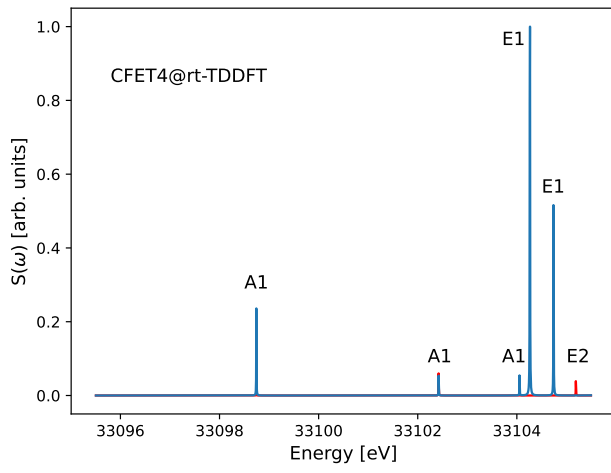
**Table 5** Deviations ( $\Delta\Delta E$  in eV) of CFET4@RT-TDDFT and oCFET4@RT-TDDFT from LR-TDDFT ( $\Delta E$  in eV) for the  $L$ -edge core excitations of HI\*

functional	term	$\Delta E$	oscillator strength	$\Delta\Delta E$ (CFET4)	$\Delta\Delta E$ (oCFET4)
HF	$A_1(\Sigma^+)$	5285.46	0.0009	0.00	0.00
	$A_1(\Sigma^+)$	5289.06	0.0000	0.00	0.00
	$A_1(\Sigma^+)$	5290.65	0.0003	0.00	0.00
	$E_1(\Pi)$	5290.87	0.0001	0.00	0.00
	$E_1(\Pi)$	5291.33	0.0000	0.01	0.00
	$E_2(\Lambda)$	5291.78	0.0000	0.00	0.00
	$A_1(\Sigma^+)$	5159.40	0.0006	0.00	0.00
	$A_1(\Sigma^+)$	5161.44	0.0000	0.00	0.00
	$A_1(\Sigma^+)$	5162.43	0.0002	0.00	0.00
	$E_1(\Pi)$	5162.88	0.0000	0.00	0.00
B3LYP	$E_1(\Pi)$	5163.65	0.0000	0.00	0.00
	$A_1(\Sigma^+)$	5163.91	0.0000	0.00	0.00
	$A_1(\Sigma^+)$	5128.01	0.0005	0.00	0.00
	$A_1(\Sigma^+)$	5129.71	0.0000	0.00	0.00
	$A_1(\Sigma^+)$	5130.56	0.0002	0.00	0.00
	$E_1(\Pi)$	5131.06	0.0000	0.00	0.00
	$E_1(\Pi)$	5131.99	0.0000	0.00	0.00
	$A_1(\Sigma^+)$	5132.03	0.0000	0.00	0.00

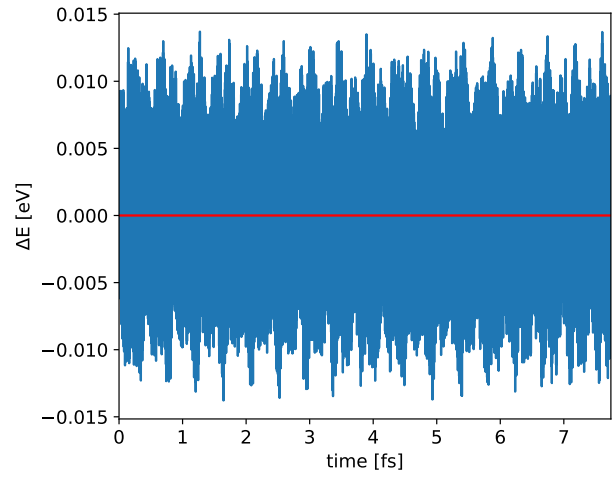
\* The  $E_2$  state can only be obtained by adding a constant perturbation to the electric field (see the text).

**Table 6** Deviations ( $\Delta\Delta E$  in eV) of MP2@RT-TDDFT/HF from LR-TDDFT/HF ( $\Delta E$  in eV) for the low-lying bright valence excitations of HI

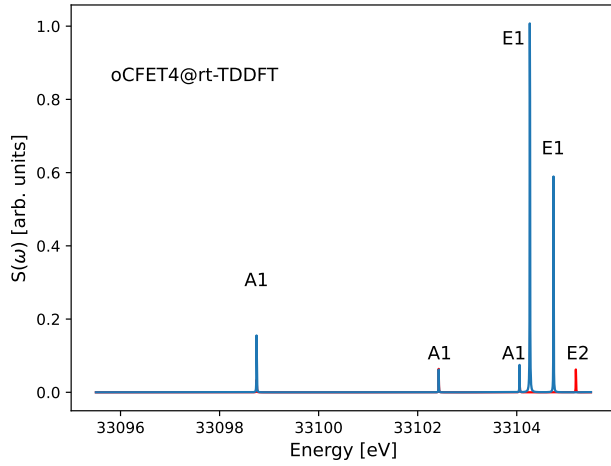
term	$\Delta E$	oscillator strength	$\Delta\Delta E$
$E_1(\Pi)$	6.22	0.0364	0.00
$E_1(\Pi)$	7.89	0.4222	0.00
$E_1(\Pi)$	8.76	0.0401	0.00
$A_1(\Sigma^+)$	9.47	0.0038	0.00



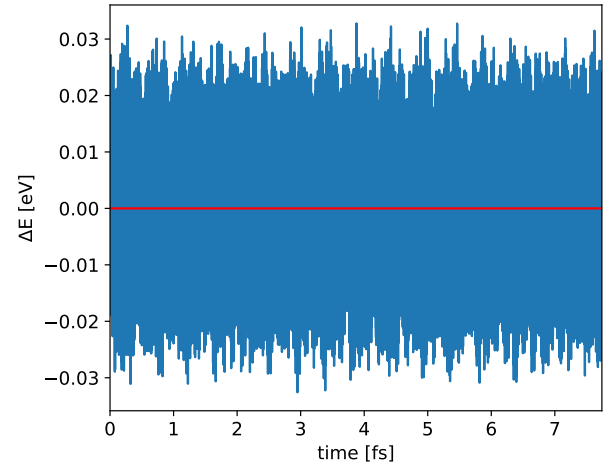
(a)



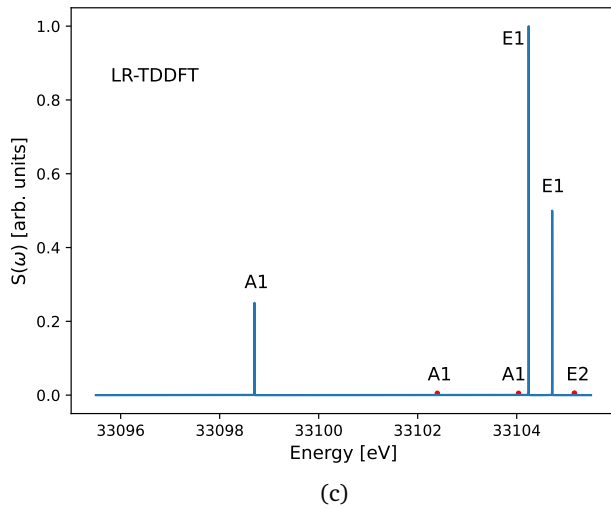
(a)



(b)



(b)



(c)

**Fig. 6** K-edge absorption spectra of HI simulated by CFET4@RT-TDDFT/HF, oCFET4@RT-TDDFT/HF and LR-TDDFT/HF. Red dots/sticks denote dark states.

**Fig. 5** Energy conservation errors  $\Delta E = E(t_{k+1}) - E(t_k)$  for (a) CFET4@RT-TDDFT/HF and (b) oCFET4@RT-TDDFT/HF.

TDDFT, even beyond the linear response regime.

## Conflicts of interest

There are no conflicts to declare.

## Acknowledgements

This work was supported by the Key-Area Research and Development Program of Guangdong Province (Grant No. 2020B0101350001), National Natural Science Foundation of China (Grant Nos. 21833001 and 21973054), and Mountain Tai Climbing Program of Shandong Province.

## Data Availability Statement

The data that supports the findings of this study is available within the article.

## Notes and references

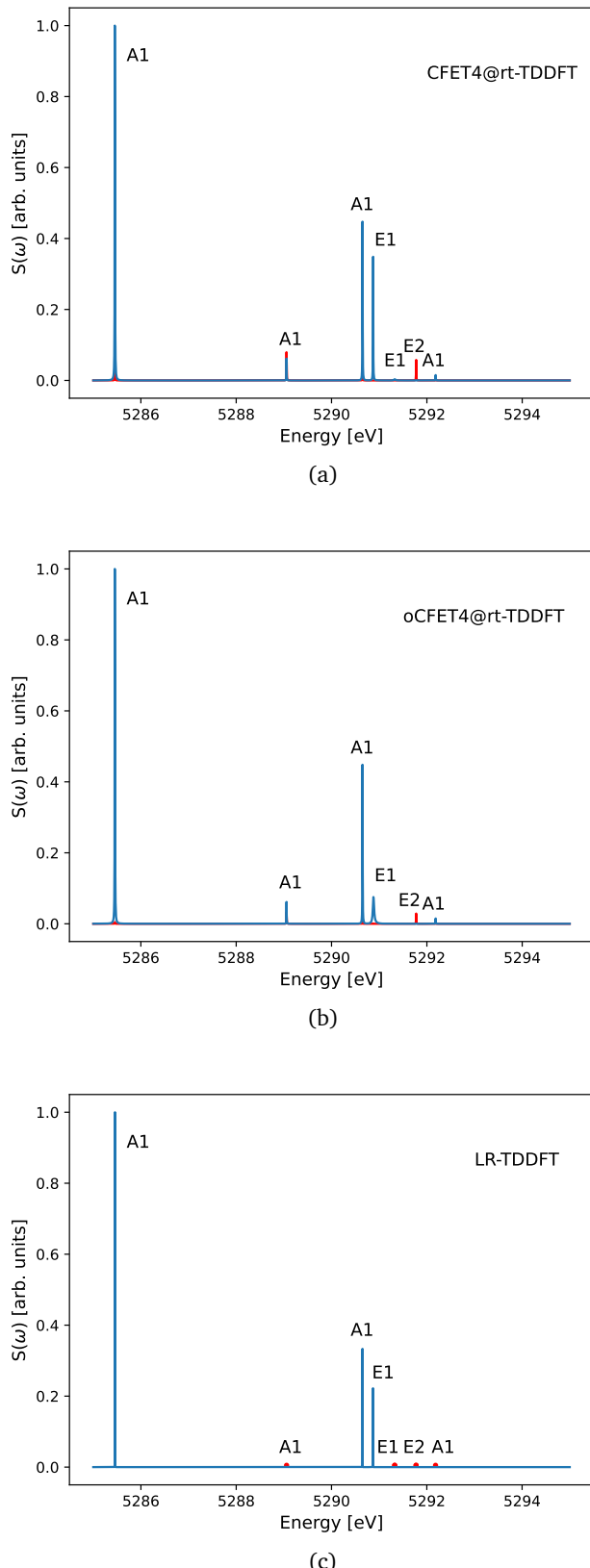


**Fig. 7** L-edge absorption spectra of HI simulated by CFET4@RT-TDDFT/HF, oCFET4@RT-TDDFT/HF and LR-TDDFT/HF. Red dots/sticks denote dark states.

- 1 P. Norman and A. Dreuw, *Chem. Rev.*, 2018, **118**, 7208–7248.
- 2 J. Gao, A. Grofe, H. Ren and P. Bao, *J. Phys. Chem. Lett.*, 2016, **7**, 5143–5149.
- 3 A. Grofe, X. Chen, W. Liu and J. Gao, *J. Phys. Chem. Lett.*, 2017, **8**, 4838–4845.
- 4 L. Yang, A. Grofe, J. Reimers and J. Gao, *Chem. Phys. Lett.*, 2019, **736**, 136803.
- 5 R. Zhao, A. Grofe, Z. Wang, P. Bao, X. Chen, W. Liu and J. Gao, *J. Phys. Chem. Lett.*, 2021, **12**, 7409–7417.
- 6 A. T. Gilbert, N. A. Besley and P. M. Gill, *J. Phys. Chem. A*, 2008, **112**, 13164–13171.
- 7 J. Liu, Y. Zhang and W. Liu, *J. Chem. Theory Comput.*, 2014, **10**, 2436–2448.
- 8 W. D. Derricotte and F. A. Evangelista, *Phys. Chem. Phys. Chem.*, 2015, **17**, 14360–14374.
- 9 Y. Liang, J. Vinson, S. Pemmaraju, W. S. Drisdell, E. L. Shirley and D. Prendergast, *Phys. Rev. Lett.*, 2017, **118**, 096402.
- 10 W. D. Derricotte and F. A. Evangelista, *J. Chem. Theory Comput.*, 2017, **13**, 5984–5999.
- 11 M. S. Oakley and M. Klobukowski, *J. Electron Spectrosc. Relat. Phenom.*, 2018, **227**, 44–50.
- 12 C. Ehlert and T. Klamroth, *J. Comput. Chem.*, 2020, **41**, 1781–1789.
- 13 K. Carter-Fenk and J. M. Herbert, *J. Chem. Theory Comput.*, 2020, **16**, 5067–5082.
- 14 J. A. Shea, E. Gwin and E. Neuscamman, *J. Chem. Theory Comput.*, 2020, **16**, 1526–1540.
- 15 D. Hait and M. Head-Gordon, *J. Chem. Theory Comput.*, 2020, **16**, 1699–1710.
- 16 A. Grofe, R. Zhao, A. Wildman, T. F. Stetina, X. Li, P. Bao and J. Gao, *J. Chem. Theory Comput.*, 2020, **17**, 277–289.
- 17 G. Fronzoni, M. Stener, A. Reduce and P. Decleva, *J. Phys. Chem. A*, 2004, **108**, 8467–8477.
- 18 M. Stener, G. Fronzoni and M. d. de Simone, *Chem. Phys. Lett.*, 2003, **373**, 115–123.
- 19 K. Ray, S. DeBeer George, E. I. Solomon, K. Wieghardt and F. Neese, *Chem.-Eur. J.*, 2007, **13**, 2783–2797.
- 20 N. A. Besley and F. A. Asmurf, *Phys. Chem. Chem. Phys.*, 2010, **12**, 12024–12039.
- 21 W. Liang, S. A. Fischer, M. J. Frisch and X. Li, *J. Chem. Theory Comput.*, 2011, **7**, 3540–3547.
- 22 B. E. Van Kuiken, N. Huse, H. Cho, M. L. Strader, M. S. Lynch, R. W. Schoenlein and M. Khalil, *J. Phys. Chem. Lett.*, 2012, **3**, 1695–1700.
- 23 Z. Li and W. Liu, *J. Chem. Phys.*, 2010, **133**, 064106.
- 24 Z. Li, W. Liu, Y. Zhang and B. Suo, *J. Chem. Phys.*, 2011, **134**, 134101.
- 25 Z. Li and W. Liu, *J. Chem. Phys.*, 2011, **135**, 194106.
- 26 B. E. Van Kuiken, M. Valiev, S. L. Daifuku, C. Bannan, M. L.

Strader, H. Cho, N. Huse, R. W. Schoenlein, N. Govind and M. Khalil, *J. Phys. Chem. A*, 2013, **117**, 4444–4454.

27 P. Verma, W. D. Derricotte and F. A. Evangelista, *J. Chem. Theory Comput.*, 2016, **12**, 144–156.

28 R. Peng, A. V. Copan and A. Y. Sokolov, *TJ. Phys. Chem. A*, 2019, **123**, 1840–1850.

29 A. Nenov, F. Segatta, A. Bruner, S. Mukamel and M. Garavelli, *J. Chem. Phys.*, 2019, **151**, 114110.

30 K. Lopata, B. E. Van Kuiken, M. Khalil and N. Govind, *J. Chem. Theory Comput.*, 2012, **8**, 3284–3292.

31 K. Lopata and N. Govind, *J. Chem. Theory Comput.*, 2013, **9**, 4939–4946.

32 R. G. Fernando, M. C. Balhoff and K. Lopata, *J. Chem. Theory Comput.*, 2015, **11**, 646–654.

33 A. Sissay, P. Abanador, F. Mauger, M. Gaarde, K. J. Schafer and K. Lopata, *J. Chem. Phys.*, 2016, **145**, 094105.

34 A. Bruner, D. LaMaster and K. Lopata, *J. Chem. Theory Comput.*, 2016, **12**, 3741–3750.

35 S. P. Neville and M. S. Schuurman, *J. Chem. Phys.*, 2018, **149**, 154111.

36 M. Chen and K. Lopata, *J. Chem. Theory Comput.*, 2020, **16**, 4470–4478.

37 X. Li, N. Govind, C. Isborn, A. E. DePrince III and K. Lopata, *Chem. Rev.*, 2020, **120**, 9951–9993.

38 M. Yang, A. Sissay, M. Chen and K. Lopata, *J. Chem. Theory Comput.*, 2022.

39 P. Verma and R. J. Bartlett, *J. Chem. Phys.*, 2016, **145**, 034108.

40 F. Zapata, E. Luppi and J. Toulouse, *J. Chem. Phys.*, 2019, **150**, 234104.

41 J. Gao, W. Liu, B. Song and C. Liu, *J. Chem. Phys.*, 2004, **121**, 6658–6666.

42 J. Gao, W. Zou, W. Liu, Y. Xiao, D. Peng, B. Song and C. Liu, *J. Chem. Phys.*, 2005, **123**, 054102.

43 R. Bast, H. J. A. Jensen and T. Saue, *Int. J. Quantum Chem.*, 2009, **109**, 2091–2112.

44 S. Komorovsky, P. J. Cherry and M. Repisky, *J. Chem. Phys.*, 2019, **151**, 184111.

45 L. Konecny, M. Repisky, K. Ruud and S. Komorovsky, *J. Chem. Phys.*, 2019, **151**, 194112.

46 F. Wang, T. Ziegler, E. van Lenthe, S. van Gisbergen and E. J. Baerends, *J. Chem. Phys.*, 2005, **122**, 204103.

47 D. Peng, W. Zou and W. Liu, *J. Chem. Phys.*, 2005, **123**, 144101.

48 W. Xu, J. Ma, D. Peng, W. Zou, W. Liu and V. Staemmler, *Chem. Phys.*, 2009, **356**, 219–228.

49 W. Xu, Y. Zhang and W. Liu, *Sci. China Ser. B-Chem.*, 2009, **52**, 1945–1953.

50 M. Kühn and F. Weigend, *J. Chem. Theory Comput.*, 2013, **9**, 5341–5348.

51 M. Kühn and F. Weigend, *J. Chem. Phys.*, 2014, **141**, 224302.

52 K. Mori, T. Goumans, E. Van Lenthe and F. Wang, *Phys. Chem. Chem. Phys.*, 2014, **16**, 14523–14530.

53 F. Egidi, J. J. Goings, M. J. Frisch and X. Li, *J. Chem. Theory Comput.*, 2016, **12**, 3711–3718.

54 F. Egidi, S. Sun, J. J. Goings, G. Scalmani, M. J. Frisch and X. Li, *J. Chem. Theory Comput.*, 2017, **13**, 2591–2603.

55 T. F. Stetina, J. M. Kasper and X. Li, *J. Chem. Phys.*, 2019, **150**, 234103.

56 W. Liu and Y. Xiao, *Chem. Soc. Rev.*, 2018, **47**, 4481–4509.

57 M. Repisky, L. Konecny, M. Kadek, S. Komorovsky, O. L. Malkin, V. G. Malkin and K. Ruud, *J. Chem. Theory Comput.*, 2015, **11**, 980–991.

58 L. Konecny, M. Kadek, S. Komorovsky, K. Ruud and M. Repisky, *J. Chem. Phys.*, 2018, **149**, 204104.

59 M. De Santis, L. Storchi, L. Belpassi, H. M. Quiney and F. Tarantelli, *J. Chem. Theory Comput.*, 2020, **16**, 2410–2429.

60 J. J. Goings, J. M. Kasper, F. Egidi, S. Sun and X. Li, *J. Chem. Phys.*, 2016, **145**, 104107.

61 L. Konecny, M. Kadek, S. Komorovsky, O. L. Malkina, K. Ruud and M. Repisky, *J. Chem. Theory Comput.*, 2016, **12**, 5823–5833.

62 J. M. Kasper, P. J. Lestrange, T. F. Stetina and X. Li, *J. Chem. Theory Comput.*, 2018, **14**, 1998–2006.

63 J. M. Kasper, T. F. Stetina, A. J. Jenkins and X. Li, *Chem. Phys. Rev.*, 2020, **1**, 011304.

64 P. Darapaneni, A. M. Meyer, M. Sereda, A. Bruner, J. A. Dorman and K. Lopata, *J. Chem. Phys.*, 2020, **153**, 054110.

65 M. E. Casida, in *Time-Dependent Density Functional Response Theory for Molecules*, ed. D. P. Chong, WORLD SCIENTIFIC, 1995, pp. 155–192.

66 D. Peng, J. Ma and W. Liu, *Int. J. Quantum Chem.*, 2009, **109**, 2149–2167.

67 C. Huang, W. Liu, Y. Xiao and M. R. Hoffmann, *J. Comput. Chem.*, 2017, **38**, 2481–2499.

68 C. Huang and W. Liu, *J. Comput. Chem.*, 2019, **40**, 1023–1037.

69 S. P. Neville and M. S. Schuurman, *J. Chem. Phys.*, 2019, **150**, 184115.

70 M. F. Herbst and T. Fransson, *J. Chem. Phys.*, 2020, **153**, 054114.

71 R. Kosloff, *J. Phys. Chem.*, 1988, **92**, 2087–2100.

72 A. Castro, M. A. Marques and A. Rubio, *J. Chem. Phys.*, 2004, **121**, 3425–3433.

73 A. Gomez Pueyo, M. A. Marques, A. Rubio and A. Castro, *J. Chem. Theory Comput.*, 2018, **14**, 3040–3052.

74 W. Magnus, *Commun. Pur. Appl. Math.*, 1954, **7**, 649–673.

75 A. Alvermann and H. Fehske, *J. Comput. Phys.*, 2011, **230**, 5930–5956.

76 S. Blanes, F. Casas, J.-A. Oteo and J. Ros, *Phys. Rep.*, 2009, **470**, 151–238.

77 S. Blanes and P. C. Moan, *App. Num. Math.*, 2006, **56**, 1519–1537.

78 W. Liu, *J. Chem. Phys.*, 2020, **152**, 180901.

79 W. Liu, *Sci. Sin. Chim.*, 2020, **50**, 1672–1696.

80 R. Baer and D. Neuhauser, *J. Chem. Phys.*, 2004, **121**, 9803–

9807.

81 F. Wang, C. Y. Yam, G. Chen and K. Fan, *J. Chem. Phys.*, 2007, **126**, 134104.

82 C.-L. Cheng, J. S. Evans and T. Van Voorhis, *Phys. Rev. B*, 2006, **74**, 155112.

83 Y. Zhu and J. M. Herbert, *J. Chem. Phys.*, 2018, **148**, 044117.

84 H. Nyquist, *Transactions of the American Institute of Electrical Engineers*, 1928, **47**, 617–644.

85 C. E. Shannon, *Bell System Technical Journal*, 1948, **27**, 379–423.

86 M. R. Wall and D. Neuhauser, *J. Chem. Phys.*, 1995, **102**, 8011–8022.

87 V. A. Mandelshtam and H. S. Taylor, *J. Chem. Phys.*, 1997, **107**, 6756–6769.

88 J. W. Pang, T. Dieckmann, J. Feigon and D. Neuhauser, *J. Chem. Phys.*, 1998, **108**, 8360–8368.

89 Z. Li, Y. Xiao and W. Liu, *J. Chem. Phys.*, 2012, **137**, 154114.

90 Z. Li, Y. Xiao and W. Liu, *J. Chem. Phys.*, 2014, **141**, 054111.

91 W. Kutzelnigg and W. Liu, *J. Chem. Phys.*, 2005, **123**, 241102.

92 W. Liu and D. Peng, *J. Chem. Phys.*, 2009, **131**, 031104.

93 A. D. Becke, *J. Chem. Phys.*, 1993, **98**, 5648–5652.

94 P. J. Stephens, F. J. Devlin, C. F. Chabalowski and M. J. Frisch, *J. Phys. Chem.*, 1994, **98**, 11623–11627.

95 A. D. Becke, *Phys. Rev. A*, 1988, **38**, 3098–3100.

96 C. Lee, W. Yang and R. G. Parr, *Phys. Rev. B*, 1988, **37**, 785–789.

97 P. J. P. de Oliveira, C. L. Barros, F. E. Jorge, A. C. Neto and M. Campos, *J. Mol. Struc.-THEOCHEM*, 2010, **948**, 43–46.

98 W. Liu, G. Hong, D. Dai, L. Li and M. Dolg, *Theor. Chem. Acc.*, 1997, **96**, 75–83.

99 W. Liu, F. Wang and L. Li, *J. Theor. Comput. Chem.*, 2003, **2**, 257–272.

100 W. Liu, F. Wang and L. Li, in *Relativistic Density Functional Theory: The BDF Program Package*, ed. K. Hirao and Y. Ishikawa, World Scientific, Singapore, 2004, pp. 257–282.

101 Y. Zhang, B. Suo, Z. Wang, N. Zhang, Z. Li, Y. Lei, W. Zou, J. Gao, D. Peng, Z. Pu, Y. Xiao, Q. Sun, F. Wang, Y. Ma, X. Wang, Y. Guo and W. Liu, *J. Chem. Phys.*, 2020, **152**, 064113.